

1 Encephalomyocarditis virus protein 2B* antagonises innate immune signalling by
2 interacting with 14-3-3 protein family members

3

4 Samantha K. Nguyen^a, Stephen Holmes^b, Henry G. Barrow^{a1}, Nina Lukhovitskaya^a,
5 Aminu S. Jahun^{a2}, Iliana Georgana^{a3}, Laura G. Caller^a, James R. Edgar^a, Edward
6 Emmott^b, Andrew E. Firth^{a#}, Hazel Stewart^{a#}.

7

8 ^aDepartment of Pathology, University of Cambridge, Cambridge, United Kingdom.

9 ^bCentre for Proteome Research, Department of Biochemistry, Cell & Systems Biology,
10 Institute of Systems, Molecular and Integrative Biology, University of Liverpool,
11 Liverpool, United Kingdom.

12 ¹Present address: Cambridge Institute for Medical Research, Department of Clinical
13 Neurosciences, University of Cambridge, Cambridge, United Kingdom.

14 ²Present address: MRC Laboratory of Molecular Biology, Francis Crick Avenue,
15 Cambridge, United Kingdom.

16 ³Present address: Scientific Research and Innovation, Medicines and Healthcare
17 Products Regulatory Agency, South Mimms, United Kingdom.

18

19 #Address correspondence to Hazel Stewart (hs623@cam.ac.uk) and Andrew E. Firth
20 (aef24@cam.ac.uk).

21 *Running title: 2B* interacts with 14-3-3s to target immune signalling*

22 *Abstract word count: 191*

23 *Main text word count: 4290 excluding Methods, References and Figure legends*

24 **ABSTRACT**

25 Encephalomyocarditis virus (EMCV) has for decades served as an important model
26 RNA virus. Although most of the EMCV proteins are obtained via proteolytic cleavage of
27 a long polyprotein, 2B* is expressed from a short overlapping open reading frame via an
28 unusual protein-stimulated temporally dependent ribosomal frameshifting mechanism.
29 The function of 2B* has not yet been characterised, though mutant viruses that are
30 unable to express 2B* have a small plaque phenotype. Here we show that 2B* binds all
31 seven members of the 14-3-3 protein family during virus infection. Binding is dependent
32 on the 2B* C-terminal sequence RRNSS. IFN- β and IL-6 signalling are impeded
33 following overexpression of 2B* but not a truncated version lacking the RRNSS
34 residues, thus suggesting a 14-3-3-dependent role for 2B* in inhibiting MAVS signalling.
35 We also find that this function is distinct from the effect of 2B* on plaque size, as a virus
36 in which 2B* was similarly truncated exhibited near-wildtype plaque size, thus indicating
37 that 2B* also harbours additional functions. This work provides the first identification of a
38 role of 2B* in innate immune antagonism and expands our knowledge of the protein
39 complement of this important model virus.

40

41 **IMPORTANCE**

42 Encephalomyocarditis virus (EMCV) infects a range of species, causing economically
43 important reproductive disorders in pigs and encephalitis and myocarditis in rodents.
44 Due to its wide host range, it is an important model pathogen for investigating virus-host
45 interactions. EMCV expresses an accessory protein, 2B*, from an overlapping open
46 reading frame via an unusual ribosomal frameshifting mechanism. Although the

47 frameshifting mechanism has been established, the function of the 2B* protein had not
48 previously been explored. Here, we determined the host proteins to which 2B* binds
49 and found that it specifically binds to the entire 14-3-3 protein family which, among other
50 roles, contribute to the innate immune response to viral infection in mammalian cells.
51 This interaction requires a specific stretch of amino acids at the end of 2B*. By
52 interacting with the 14-3-3 proteins, 2B* blocks immune response activation. Thus, 2B*
53 is a novel antagonist of innate immunity.

54

55 **KEYWORDS**

56 Picornavirus, EMCV, interferon beta, cardiovirus, ribosome frameshifting, innate
57 immunity, proteomics, 14-3-3 proteins, 2B*.

58

59 **INTRODUCTION**

60

61 Encephalomyocarditis virus (EMCV) is a positive-sense single-stranded RNA virus in
62 the genus *Cardiovirus* of the family *Picornaviridae*. EMCV causes encephalitis and
63 myocarditis in a variety of species, as well as reproductive disorders in pigs. The
64 genome is approximately 8 kb in length and encodes a long polyprotein which is
65 cleaved to produce 12 mature virus proteins. Although most of the polyprotein
66 processing is performed by the viral 3C protease, separation between 2A and 2B occurs
67 via the StopGo mechanism whereby a specific amino acid sequence ending in NPGP
68 co-translationally prevents formation of a peptide bond between the G and the final P
69 (1). Just 12 codons downstream of the 2A|2B junction, lies a programmed ribosomal
70 frameshifting (PRF) site at which a proportion of ribosomes are stimulated to make a -1
71 nt shift into the 117-codon overlapping 2B* open reading frame (ORF) (2). The shift site
72 comprises a G GUU UUU heptanucleotide (spaces separate polyprotein-frame codons),
73 and the stimulator comprises a 3' RNA structure that binds the viral 2A protein to form
74 an RNA:protein complex that impedes ribosome processivity (3, 4). Ribosomes which
75 make a -1 nt shift can more efficiently remove 2A and unwind this RNA structure to
76 continue translation (3). PRF leads to the production of the 129 amino acid "transframe"
77 protein 2B*, and prevents translation of the downstream nonstructural proteins. The
78 efficiency of PRF is regulated by the increasing concentration of 2A over time, with the
79 percentage of frameshifting ribosomes increasing from 0% at 2 h post infection (h p.i.)
80 to ~70% at 6–8 h p.i. (3). Thus both the expression level of 2B* and the ratio of
81 structural to nonstructural proteins are temporally controlled.

82

83 Although the amino acid sequence of 2B* is highly conserved between EMCV isolates,
84 it is not encoded by other picornaviruses, even the closely related cardiovirus, Theiler's
85 murine encephalomyelitis virus (TMEV). Although PRF does occur at the same site in
86 TMEV, it leads to the expression of a peptide only 14 residues in length that has no
87 known function (5). Therefore, in TMEV it is thought that PRF is used purely as a
88 "ribosome sink" to temporally control the ratio of structural to nonstructural protein
89 synthesis (5, 6). 2B* therefore represents an entirely uncharacterised protein, present in
90 a subgroup of cardioviruses. The loss of 2B* has been associated with reduced viral
91 plaque size (2, 3), however the molecular mechanisms responsible for this have not yet
92 been elucidated.

93

94 Here, we modified the EMCV genome to encode an HA-tagged 2B* protein. Using this
95 virus, we identified the host protein binding partners of 2B* and found that they include
96 the entire family of 14-3-3 proteins. A short linear motif at the C terminus of 2B* is
97 essential for 14-3-3 binding. Interaction of 2B* with the 14-3-3 members reduced
98 transcription of both *IFNB1* and *IL6* in addition to interferon stimulated gene (ISG)
99 transcripts, in accordance with recently published results describing a role of 14-3-3
100 proteins in promoting antiviral immunity (7-10). This antagonism of the innate immune
101 system, via sequestration of the 14-3-3 family, is distinct from the previously described
102 role of 2B* in promoting plaque size, thus indicating that 2B* possesses multiple
103 functions which contribute to efficient EMCV replication and transmission.

104

105

106 **RESULTS**

107

108 **Identification of a 2B*KO EMCV mutation that does not affect viral frameshifting**
109 **or replication**

110

111 As the ORF of 2B* overlaps the coding sequence of 2B, we first sought to confirm that
112 mutations applied to create a 2B* knock-out (2B*KO) virus do not affect either viral PRF
113 efficiency or RNA replication. Several 2B*KO EMCV mutants have been described
114 previously (2, 11), one of which possesses two stop codons immediately after the RNA
115 stem-loop, which are synonymous in the 2B reading frame (WT-PTC mutant of Ling et
116 al., 2017). In this virus, PRF results in expression of a severely truncated, 29 residue N-
117 terminal fragment of the 129 residue 2B*.

118

119 As PRF in EMCV directs ribosomes out of the polyprotein reading frame into the 2B*
120 reading frame, any effect of the 2B*KO mutation on PRF efficiency would affect the ratio
121 of structural to nonstructural protein synthesis at late stages of infection, potentially
122 overshadowing any phenotype caused by the loss of 2B*. While previous work with a
123 metabolic labelling assay (11) indicated that the same 2B*KO mutation did not have a
124 measurable effect on frameshifting, we sought to confirm this with an alternative, dual
125 luciferase-based assay (Figure 1A, 1B).

126

127 For each sequence tested, the shift site, stem loop and any downstream mutations were
128 inserted into the previously described pSGDLuc plasmid (12). The resulting plasmids
129 contained 11 nt upstream of the slippery sequence, the 7 nt slippery sequence itself and
130 an additional downstream 87 nt, between renilla and firefly luciferase ORFs which were
131 in the same reading frame (0 frame) (Figure 1A). Flanking the inserted nucleotides were
132 two FMDV StopGo sequences, enabling co-translational separation, to ensure that the
133 peptide sequences encoded by the insert are not tagged onto the end of the renilla
134 and/or firefly luciferases where they might differentially affect enzymatic activities.

135 Ribosomes which do not frameshift translate both luciferase proteins whereas
136 ribosomes which frameshift translate only the renilla luciferase (Figure 1A).

137
138 As binding of the EMCV 2A protein to the stem-loop is necessary for PRF, a construct
139 encoding FLAG-tagged EMCV 2A (pCAGG-2A) was co-transfected with each pSGDLuc
140 construct. To allow normalisation of the relative luciferase readings, each pSGDLuc
141 construct was also co-transfected with a plasmid encoding a FLAG-tagged 2A mutant
142 (pCAGG-2Amut) that is unable to bind the stem-loop and unable to stimulate PRF (3).

143 The PRF efficiency could then be calculated as $1 - \frac{(\text{FLuc}_{\text{test}}/\text{RLuc}_{\text{test}})/(\text{FLuc}_{\text{2Amut}}/\text{RLuc}_{\text{2Amut}})}$. As the ratio of pCAGG-2A to pSGDLuc which
144 would mimic the ratio of 2A protein to viral RNA occurring in infection was unknown, a
145 range of co-transfection ratios were performed (Figure 1B).

146
147
148 A previously described mutant sequence, non-permissive to PRF due to mutations in
149 both the slippery sequence and stem-loop (SS-SL) (3) , was also inserted in the

150 pSGDLuc vector as an additional control. A further single-nucleotide insertion was
151 added to this construct to create –1 SS-SL. Here, the SS-SL mutations prevented PRF
152 and the insertion caused all ribosomes to enter the 2B*-derived reading frame, thus
153 mimicking 100% PRF. As expected, pSGDLuc-2B*KO showed no significant difference
154 in PRF efficiency compared to pSGDLuc-WT, indicating that the 2B*KO mutations do
155 not affect PRF and therefore any phenotypic differences found between 2B*KO EMCV
156 and WT EMCV in later experiments would not be due to impaired PRF efficiency.

157
158 In principle, any change to the viral RNA genome may also influence viral RNA
159 replication. 2B* mutant viruses have previously been observed to reach equivalent
160 overall titres to WT (2). Furthermore, 2B* is only expressed at late time points, after
161 substantial amounts of RNA replication have already occurred. Therefore any difference
162 in viral replication rates between 2B*KO EMCV and WT EMCV would likely be due to
163 changes in RNA sequence or RNA structure, rather than a direct function of the 2B*
164 protein. To further validate the use of 2B*KO EMCV as a tool for later studies, we
165 investigated the effect of the 2B*KO mutations on viral replication using a GFP-tagged
166 virus (GFP WT EMCV) (13), which contains the GFP ORF immediately followed by the
167 EMCV 3C protease cleavage site, upstream of the leader and capsid proteins. The
168 essential GDD motif in the viral RNA polymerase, 3D, was mutated to GNN to create a
169 replication incompetent control. The GNN mutation and the 2B*KO mutation were
170 independently introduced into the parental genome, creating GFP GNN EMCV and GFP
171 2B*KO EMCV, respectively. Following infection, the increasing levels of GFP in an

172 infected cell would be directly proportional to the amount of viral protein produced and
173 hence a reflection of viral replication.

174
175 BHK-21 cells were infected with these viruses and viral replication over time was
176 measured by live-cell imaging (Figure 1C). Green calibrated units (GCU) at each
177 timepoint were normalised to the GCU in that sample at 5.5 h p.i., which was when GFP
178 was first detectable in most samples. As cell lysis occurred at approximately 8 h p.i.
179 (one viral replication cycle), GFP was not measured past this point. The fold change in
180 GCU was not significantly different between cells infected with GFP WT EMCV or GFP
181 2B*KO EMCV at any of the timepoints measured (Figure 1C) while GFP GNN EMCV
182 consistently gave only background levels of GCU. Thus the 2B*KO mutations do not
183 appear to affect viral replication. Therefore, any differences found between 2B*KO
184 EMCV and WT EMCV are unlikely to be caused by defects in either PRF or viral
185 replication and are likely to be solely attributable to the loss of 2B* protein.

186

187 **Characterisation of a virus expressing HA-tagged 2B***

188
189 Next we modified the EMCV genome to encode 2B* with an N-terminal HA tag (HA2B*
190 EMCV). This would allow 2B* to be immunoprecipitated from infected samples, and the
191 subsequent identification of its binding partners. The HA tag and a short Gly-Ser flexible
192 linker was encoded immediately following the final proline of the StopGo sequence,
193 responsible for separating 2A from 2B/2B* (Figure 2A). A similar approach has been
194 previously described to tag 2B* with a V5 epitope (11). As 2B and 2B* share the first 12

195 residues prior to the change in reading frame, both 2B and 2B* will be translated with
196 the N-terminal HA tag. However, the viral 3C protease is thought to cleave the N
197 terminus of 2B, thereby removing the tag (1, 11). The KO mutations were also
198 introduced into HA2B* EMCV to create an equivalent KO mutant virus.

199

200 At both 8 and 10 h p.i., HA2B* EMCV produced detectable levels of HA-tagged 2B* in
201 BHK-21 cells (Figure 2B). Noticeably, HA-tagged 2B was not detected in any of the
202 lysates (predicted molecular mass 13 kDa), indicating that the HA epitope was indeed
203 cleaved from the majority of 2B as expected.

204

205 To ensure that the addition of the HA tag did not disable the function of 2B* and that
206 HA2B* KO EMCV recreated the small plaque phenotype associated with the loss of 2B*
207 (2, 3), the plaques produced by each virus at 48 h p.i. in BSR cells were measured
208 (Figure 2C, 2D). Although HA2B* EMCV created smaller plaques than untagged WT
209 EMCV (median areas 2694 pixels and 6140 pixels, respectively) (Figure 2D), they were
210 still significantly larger than those of 2B*KO EMCV (median area 451 pixels). The
211 decreased size of HA2B* EMCV plaques indicated that the addition of the tag did
212 somewhat affect 2B* function. However this change was modest and, as the plaques
213 were still substantially larger than those created by 2B*KO EMCV, it is likely that HA-
214 tagged 2B* still interacts with the relevant factors required for the large plaque
215 phenotype. Therefore, HA2B* EMCV was used as a tool to characterise the interaction
216 partners of 2B*.

217

218 **Mass spectrometry identifies 14-3-3 protein family members as putative
219 interaction partners of 2B***

220

221 To identify the host and viral protein interactions of 2B*, HA2B* was immunoprecipitated
222 from HA2B* EMCV infected BHK-21 cells at 7 h p.i. in triplicate. Immunoprecipitated
223 samples were then subjected to trypsin digestion and labelling by tandem-mass-tagging
224 (TMT) prior to being analysed by liquid chromatography with tandem mass spectrometry
225 (LC-MS/MS) (Figure 3A). While the predominant tagged viral protein was 2B*, the
226 StopGo mechanism is approximately 94% efficient in EMCV and therefore small
227 amounts of HA-tagged 2A-fusion products (2AHA2B* and 2AHA2B^N, where 2B^N
228 represents the N-terminal fragment of 2B upstream of the 3C protease cleavage site
229 (11) were produced (Figure 3B). To ensure any interacting proteins bound to these
230 fusion products could be identified and removed from analysis, HA2B*KO EMCV
231 infected controls were included in addition to mock infected controls.

232

233 Seventeen proteins were enriched in HA2B* EMCV infected samples relative to both
234 HA2B* KO EMCV infected and mock infected samples, including HA2B* itself (Table 1,
235 Figure 3C, 3D). Candidate interaction partners were defined as those having both a
236 Student's *t*-test difference greater than 1.0 and a $-\log_2(p\text{-value})$ greater than 1.3.
237 Interestingly, this included the entire family of 14-3-3 proteins. The 14-3-3 family are
238 scaffold proteins involved in a wide range of cellular functions, including apoptosis (14,
239 15), cell cycle progression (16, 17), nuclear trafficking (18), innate immune signalling
240 (19, 20), autophagy (21) and proteasome function (22). Due to the importance of these

241 proteins in many pathways which EMCV utilises, we chose to focus on these proteins
242 for subsequent analyses.

243

244 To confirm their interaction with 2B*, a construct expressing HA2B* was co-transfected
245 into BHK-21 cells along with each construct encoding an N-terminally FLAG-tagged 14-
246 3-3 protein, cloned from BHK-21 cDNA. As 14-3-3 ϵ isoforms X1 and X2 could not be
247 distinguished by the peptides detected by mass spectrometry, both were included. The
248 14-3-3 proteins were then immunoprecipitated from the samples via the FLAG-tag.

249 Immunoprecipitated samples were subjected to SDS-PAGE and immunoblotting to
250 determine whether HA2B* was bound to these putative interaction partners (Figure 4A).
251 As tubulin β -chain was not identified by the co-immunoprecipitation mass spectrometry
252 analysis as a potential interaction partner of HA2B*, a construct encoding N-terminally
253 FLAG-tagged tubulin β -chain (FLAG-TUBB) was included as a negative control.

254

255 The interaction between 2B* and all of the 14-3-3 proteins was verified as the FLAG-
256 tagged proteins were all found to co-precipitate HA2B* (Figure 4A). These proteins are
257 therefore able to bind to 2B* both during infection and in overexpression and thus other
258 viral proteins are not required to mediate this interaction. Confocal microscopy
259 confirmed that 2B* and all 14-3-3 family members were dispersed throughout the
260 cytosol (Figures S1, S2, S3), and redistribution was not observed during co-expression.

261

262 **14-3-3 binding is mediated by a C-terminal 2B* motif and is not responsible for**
263 **the 2B*KO small plaque phenotype**

264

265 To identify the motif(s) within 2B* responsible 14-3-3 binding, we utilised the online
266 resource ELM (eukaryotic linear motifs) (23), which searches for short linear motifs
267 corresponding to known protein interaction sites. The ELM tool predicted the C-terminal
268 RRNSS sequence of 2B* to be a binding site for the 14-3-3 protein family. Indeed, this
269 was the best-scoring potential interaction site in 2B*, with a reported *p*-value of $6.4 \times$
270 10^{-5} . The C-terminal RRNSS sequence is highly conserved across EMCV strains with
271 occasional variations in the last position (to N, I or L). The known 14-3-3 binding motif is
272 highly conserved and, when at the C terminus of the binding partner in question, is
273 invariably p[S/T]-X₁₋₂-COOH with upstream arginine residues preferred (RRXp[S/T]-X₁₋
274 ₂-COOH) (where p is one or more phosphate group) (24). The 14-3-3 proteins form
275 homo- and heterodimers which bind target proteins when the penultimate serine within
276 the recognition motif is phosphorylated (24, 25), leading to translocation or
277 sequestration of the binding partner in question.

278

279 To investigate whether this sequence is indeed required for 2B*:14-3-3 binding, an
280 RRNSS truncated HA-tagged 2B* construct (HA Δ RRNSS 2B*) was engineered using a
281 R125Stop mutation, thus removing the five C-terminal residues of 2B*. This construct
282 was co-transfected into BHK-21 cells alongside each construct encoding a FLAG-
283 tagged 14-3-3 protein, and the FLAG co-immunoprecipitation assay was repeated
284 (Figure 4B). Every FLAG-tagged member of the 14-3-3 family was entirely unable to
285 bind to the co-transfected Δ RRNSS2B* mutant whereas the WT HA2B* was still
286 successfully bound by a representative 14-3-3 protein, 14-3-3 γ . This clearly

287 demonstrates that the RRNSS sequence of 2B* is essential for the 2B*:14-3-3
288 interaction and deletion of this sequence completely prevents this interaction.

289

290 We next investigated whether the lack of the 14-3-3:2B* interaction was the cause of
291 the small plaque phenotype characteristic of 2B* KO viruses (2, 3). The R125Stop
292 mutation, which is synonymous in the 2B reading frame, was introduced into the viral
293 genome, creating ΔRRNSS 2B* EMCV. To confirm that this mutation did not revert
294 during infection, the virus produced from infected BHK-21 cells was sequenced by
295 Sanger sequencing (Figure 4C). No detectable reversion was observed by 24 h p.i.

296

297 Interestingly, the small plaque phenotype associated with 2B*KO EMCV (median plaque
298 area 524 pixels) was not reproduced by ΔRRNSS 2B* EMCV (Figure 4D). Although the
299 difference between WT EMCV and ΔRRNSS 2B* EMCV plaque sizes was still
300 statistically significant, it was very modest (median areas 4516 pixels and 3577 pixels,
301 respectively). Therefore, the 2B*:14-3-3 interaction is unlikely to be responsible for the
302 increased plaque size seen in WT EMCV infection.

303

304 Presumably, the 2B*:14-3-3 interaction performs an additional function that is beneficial
305 to the virus. We hypothesised that the sequestration of 14-3-3 proteins by 2B* may
306 contribute to the evasion of innate immune signalling as other viral binding partners of
307 14-3-3 proteins – such as the 3C protease of enterovirus – are known to have similar
308 effects (7-10). During viral infection, RIG-I is relocalised from the cytosol to the
309 mitochondria by 14-3-3 ϵ which forms a complex with both RIG-I and TRIM25 (20), the

310 ubiquitin ligase essential for the antiviral function of RIG-I (26), enabling the activation of
311 MAVS on the mitochondrial membrane. In addition, 14-3-3 η is responsible for the
312 redistribution of MDA5, enabling MDA5-induced antiviral IFN- β signalling via MAVS
313 (19). As each 14-3-3 monomer has only one binding pocket, it is unlikely that 14-3-3
314 proteins bound to 2B* would be able to perform these functions. Therefore, we next
315 investigated the ability of 2B* to antagonise innate immune signalling via the 14-3-3
316 interaction.

317

318 **The 2B*:14-3-3 interaction interferes with innate immune signalling outside of the**
319 **context of infection**

320

321 MEF cells were transiently transfected with pCAGG-HA2B*, pCAGG-HA Δ RRNSS2B* or
322 empty pCAGG 24 h prior to activation of the IRF3 and NF κ B signalling pathways by
323 transfection with poly(I:C), a dsRNA mimic. After 6 h, *IFNB1*, *ISG15*, *IL6*, *RSAD2* and
324 *IFIT1* transcript levels were quantified by qRT-PCR, normalised to GAPDH mRNA using
325 the $\Delta\Delta$ CT method, and compared to those for the empty pCAGG transfected samples.
326 While overexpression of HA2B* prior to poly(I:C) stimulation significantly reduced the
327 transcription of *IFNB1*, *IL6* and the ISGs *ISG15* and *RSAD2* involved in innate immune
328 signalling (Figure 5A), this antagonistic ability was abrogated by the loss of the RRNSS
329 motif responsible for 14-3-3 binding.

330

331

332 **DISCUSSION**

333

334 In this study, we successfully engineered an EMCV genome which encodes an HA-
335 tagged 2B* protein, enabling the first characterisation of the binding partners of 2B*.
336 Whilst the addition of the tag had a modest effect upon plaque size, it did not completely
337 abrogate 2B* function (Figure 2C, 2D). We also confirmed that the 2B*KO virus had WT
338 levels of PRF and RNA replication, providing future studies with a tool for studying 2B*
339 phenotypes without the problem of confounding effects (Figure 1B, 1C). We identified
340 17 putative binding partners of 2B*, seven of which are members of the 14-3-3 family,
341 and identified the C-terminal 5 residues of 2B* as being essential for the 2B*:14-3-3
342 interaction. Finally, we determined the functional consequence of this interaction to be
343 disruption of innate immune signalling, presumably through sequestration of 14-3-3
344 proteins preventing their contribution to MDA5 and RIG-I activation (19, 20) and
345 subsequent inflammatory cytokine induction.

346

347 Upon recognition of viral RNA, MDA5 and RIG-I translocate from the cytosol to the
348 mitochondria where they activate MAVS (27), leading to NF κ B and IRF3 signalling (28)
349 and the production of antiviral cytokines including IL-6 and IFN- β , respectively. The
350 mechanisms by which picornaviruses antagonise this type I IFN signalling pathway vary
351 widely, and most species utilise multiple synergistic mechanisms exerted by different
352 viral proteins. It is therefore unsurprising that 2B* has evolved to reduce the immune
353 response to EMCV infection, despite EMCV encoding multiple other proteins with innate
354 immune inhibitory functions (namely, 2C, 3C and L). Although overexpression of 2B*
355 resulted in significant reduction of *IFNB1* and *IL6* transcription (Figure 5A), we were

356 unable to detect these transcripts by qRT-PCR in innate-competent RAW264.7 cells
357 infected with either WT EMCV or Δ RRNSS 2B* EMCV (data not shown). A possible
358 explanation is that – at least in these cells – other EMCV proteins compensate for the
359 loss of this function of 2B* and still prevent large amounts of *IL6* and *IFNB1* mRNA from
360 being produced.

361

362 To reduce recognition of dsRNA, EMCV viral protein 2C directly interacts with MDA5,
363 limiting MDA5-mediated innate immune signalling during EMCV infection (29). MDA5
364 signalling has been suggested to be further impaired during EMCV infection by EMCV
365 capsid protein VP2 (23), although the relevance of this role has yet to be confirmed in
366 virus infection. The EMCV protease 3C directly cleaves both RIG-I and TANK, further
367 limiting dsRNA recognition and promoting NF κ B signalling over IRF3 dimerisation.
368 Converging upon this effect, EMCV protein L impedes transcriptional upregulation of
369 antiviral response genes both by preventing IRF3 dimerisation and by inhibiting
370 nucleocytoplasmic trafficking of the relevant transcription factors (30). However, this is
371 not true for all cardioviruses: the L protein from some TMEV strains reduces IFN- β
372 production but only after the dimerised IRF3 has entered the nucleus (31). In addition,
373 the TMEV-specific L* protein further reduces the type I IFN response by binding to and
374 preventing the dimerisation of RNase L, preventing IRF3 activation (32, 33). The 14-3-3
375 sequestration mechanism exhibited by the 2B* protein appears distinct from these
376 previously described mechanisms in cardioviruses and therefore provides an additional
377 layer of protection for the virus from the host response.

378

379 As the presence of 2B* appeared to reduce the levels of all antiviral transcripts tested
380 (Figure 5A), we cannot eliminate the possibility that the 2B*:14-3-3 interaction causes a
381 global reduction in transcription initiation instead of specifically influencing the antiviral
382 response. However, 2B* does not have a nuclear localisation (Figure S1, S2, S3) and,
383 although the 14-3-3 proteins are involved in nuclear transport of some transcription
384 factors (18, 34), these do not include IRF3 or NF κ B which are responsible for the
385 upregulation of the target genes tested (*IL6*, *IFNB1*, *ISG15*, *IFIT1* and *RSAD2*). In
386 addition, EMCV-induced reduction of host transcription and translation (so-called host
387 shutoff) occurs from 4 h p.i., before 2B* is efficiently translated (11, 35). Therefore, it is
388 most likely that the effect is mediated prior to the nuclear import of IRF3 and NF κ B, as
389 the 2B*:14-3-3 interaction would impede the earlier translocation of both RIG-I and
390 TRIM25 by 14-3-3 ϵ (20) and MDA5 by 14-3-3 η (19) (Figure 6), in a manner similar to
391 the mechanisms exerted by the 14-3-3- binding proteins of influenza A, enteroviruses,
392 Zika virus and Epstein-Barr virus (7-10).

393
394 The 14-3-3 proteins are a family of scaffold proteins which form both homo- and
395 heterodimers, performing a plethora of roles many of which are unrelated to antiviral
396 immunity; hence many as-yet-undiscovered pathways may also be affected by 14-3-3
397 interactions with 2B*. The 14-3-3 dimeric complex can bring two 14-3-3-bound proteins
398 into proximity, to increase the chances of interaction. Conversely, they may prevent
399 interactions by sequestering proteins away from alternative interaction partners.
400 Although the binding motif is relatively conserved between all 14-3-3 proteins, each also
401 have distinct interaction partners to enable execution of specific roles. Although 2B* was

402 found to interact with the entire family of 14-3-3 proteins in our study, the relative
403 binding affinity of 2B* to each family member has not yet been investigated. It is also
404 possible that some of these interactions are indirect and are mediated by the formation
405 of 14-3-3 heterodimers. Further investigation may uncover specificity in the 2B*
406 interaction, perhaps ensuring 2B* preferentially affects particular pathways *in vivo*.
407 Binding is controlled by the phosphorylation status of the target protein, as the
408 recognition motif is only bound once phosphorylated(14); the relevance of
409 phosphorylation for 2B* function has also not yet been investigated. The 14-3-3 proteins
410 also preferentially bind to disordered regions (36) (which the C-terminus of 2B* is
411 predicted to be by analysis with Alphafold, I-TASSER and NetSurfp).

412
413 It seems counterintuitive that 2B*, a protein which is only translated at late timepoints
414 shortly before the onset of cell lysis, would have a role in preventing the antiviral
415 response. However other viruses are known to add further layers of protection against
416 innate immune signalling at later stages of infection (37-39). This is likely due to the
417 additional need for protection following the increased pathogen associated molecular
418 patterns (PAMP) exposure caused by cell death and permeabilisation of the
419 membranes: the change in cytosolic composition also induces innate immune
420 responses (40), hence there is increased risk of forewarning surrounding cells of virus
421 exposure during the lysis process. In addition, at early stages of infection EMCV
422 benefits from NF κ B activation (41) which would no longer be necessary when lysis is
423 underway. It therefore seems reasonable that 2B* could provide an additional layer of
424 protection against antiviral responses at this late stage. However, since TMEV also

425 contains the PRF signal, but not the lengthy 2B* ORF, it is likely that highly efficient
426 temporally controlled PRF evolved first as a ribosome sink to downregulate synthesis of
427 the replication proteins at late timepoints. Expansion of the 2B* ORF in the EMCV
428 lineage allowed 2B* to secondarily evolve into a functional protein in its own right. Thus,
429 late expression of 2B* may alternatively be an unavoidable consequence of the original
430 function of cardiovirus PRF and is not necessarily optimal for its role in antagonising
431 innate immune signalling.

432

433 A focus of future work will be to assess the function of the other binding partners
434 identified in our proteomics screen; it is possible that at least one of these proteins
435 contributes to the small plaque phenotype already described. The minor reduction in
436 plaque size produced by ΔRRNSS 2B* EMCV (Figure 4D) may potentially be explained
437 by a slight increase in MAVS-induced apoptosis or MAVS-induced inhibition of viral
438 spread, and clearly this interaction does not fully explain the plaque size phenotype
439 previously reported for 2B*KO viruses (2, 3).

440

441 In summary, we propose a model whereby 2B* inhibits translocation of the innate
442 immune signalling molecules MDA5, RIG-I and TRIM25 via its interaction with 14-3-3
443 proteins, thereby reducing NF κ B and IRF3 signalling. Our findings add 2B* to the
444 growing list of viral proteins, from a wide range of families, which interact with the 14-3-3
445 proteins to reduce antiviral cytokine signalling (7-10) and identify 2B* as another
446 “transframe” protein with a role in antagonising the innate immune response (37, 42,
447 43).

448

449

450 **MATERIALS AND METHODS**

451

452 Mammalian cell culture

453

454 BHK-21 (ATCC) (baby hamster kidney fibroblast), BSR (single cell clone of BHK-21
455 cells) and MEF (mouse embryonic fibroblast) cells were maintained in Dulbecco's
456 Modified Eagle Medium with high glucose (Sigma), supplemented with 10% (v/v) heat-
457 inactivated foetal calf serum (FCS), 25 mM HEPES, 2 mM L-glutamine and non-
458 essential amino acids (Sigma) ("complete DMEM") in a humidified 5% CO₂ atmosphere
459 at 37°C. All cell lines were confirmed to be mycoplasma-free at regular intervals
460 (MycoAlertTM PLUS Assay, Lonza).

461

462 RT-PCR

463

464 Uninfected BHK-21 cells, or cells infected at an MOI of 0.1, were trypsinised either 24 h
465 after plating or 24 h p.i. respectively. The trypsin was neutralised in 10% FCS DMEM
466 before the cells were pelleted at 1000 × g and the media was removed before the RNA
467 was extracted using a commercial kit as recommended (RNeasy, Qiagen). Reverse
468 transcription of each sample was carried out using 5 µg of RNA, random hexamers and
469 Superscript III reverse transcriptase (ThermoFisher Scientific). PCR using relevant
470 primers immediately followed reverse transcription.

471

472 Expression Plasmids

473

474 The pCAGG-HA2B* expression construct was originally synthesised from a gene block
475 (Integrated DNA Technologies), designed with the 2B* coding sequence from the WT
476 EMCV clone, with an additional Kozak sequence, the HA tag and a GGSGGS linker
477 sequence as well as a non-viral termination codon between *PacI* and *BglII* restriction
478 sites (sequence available upon request).

479

480 For all cellular proteins identified as being potential interaction partners of 2B* (by
481 affinity capture coupled to quantitative proteomics), corresponding coding sequences
482 were cloned from cDNA of uninfected BHK-21 cells. RNA was extracted from BHK-21
483 cells, reverse transcribed (see above) and the cDNA used for PCR amplification.
484 Primers for the PCR amplification of all constructs were designed to add to each gene
485 flanking *PacI* and either *AfI* or *BglII* restriction sites, as well as an N-terminal FLAG tag
486 separated by a GGSGGS linker. These amplicons were then digested and ligated into
487 pCAGG.

488

489 DNA transfection

490

491 BHK-21 cells were transfected at 60–70% confluence, in a 6 well plate seeded the day
492 prior. 15 µL lipofectamine 2000 (Invitrogen) was added to 300 µL Opti-MEM and a total
493 of 4 µg DNA was added into another 300 µL Opti-MEM. These solutions were then

494 mixed and incubated for 20 min while cells were washed with PBS. Following addition of
495 transfection mixture, cells were incubated for 3.5 h at 37°C with gentle agitation. 2 mL of
496 complete DMEM was then added to each well and incubated for 24 h. For all co-
497 immunoprecipitation samples, including those used for TMT mass spectrometry
498 analysis, 10 cm dishes of BHK-21 were transfected using a scaled protocol, similar to
499 that described above.

500

501 **Frameshifting assays**

502

503 For the WT sequence and each mutant to be tested, 105 nt (106 nt for –1 SS-SL)
504 covering the 2B* frameshift site (11 nt upstream, 7 nt slippery sequence, 87 nt
505 downstream) was amplified by 2-step overlap extension PCR (primer sequences
506 available upon request, numbers exclude restriction enzyme sites). Amplicons were
507 ligated into pSGDLuc via *Bg*II and *Psp*XI restriction sites. These fragments included the
508 desired mutations for testing, as well as the slippery sequence and stem-loop required
509 for frameshifting(3).

510

511 BHK-21 cells were subcultured 24 h prior to being reverse transfected with the
512 pSGDLuc plasmids in a 96 well plate. Upon reverse transfection, cells were trypsinised
513 and washed in DMEM containing 2% FCS, 25 mM HEPES and 1 mM L-glutamine and
514 washed again in DMEM with 25 mM HEPES and 1 mM L-glutamine without FCS. The
515 cells were then resuspended in this sera-free DMEM. 150 ng of total DNA and 0.5 µL
516 lipofectamine 2000 per well was incubated at room temperature in 10.5 µL of Opti-MEM

517 (Gibco) for 20 min prior to the addition of 6.5×10^4 BHK-21 cells per well. 5% FCS was
518 added, and the transfections were immediately seeded into plates in triplicate and
519 incubated for 24 h, before being frozen in 50 μ L of passive lysis buffer (Promega).
520 After thawing, 30 μ L of the lysate was sequentially mixed with 30 μ L of each luciferase
521 reagent (Promega) as described by the manufacturer.

522

523 **Quantitative RT-PCR**

524

525 Following transfection of MEF cells, the media was changed prior to addition of Opti-
526 MEM with lipofectamine 2000 (Invitrogen) and poly(I:C) to a final concentration of 10
527 μ g/mL poly(I:C). After 6 h RNA was extracted and 1 μ g of total RNA was used for
528 reverse transcription (Quantitect reverse transcription kit, Qiagen) as per instructions.
529 cDNA was amplified using a ViiA 7 real-time PCR system (ThermoFisher Scientific).
530 The reaction cycle threshold was determined using the following program: i) initial
531 heating to 55°C for 2 min; ii) initial denaturation for 10 min at 95°C; iii) 40 cycles of
532 denaturation for 15 s at 95°C, annealing for 1 min at 60°C. The melt curve was
533 calculated by denaturation for 15 s at 95°C, annealing for 1 min at 60°C with 0.05°C
534 increments to 95°C. The primer sequences for mouse IL6 were (sense) 5'
535 GAAGTCCCTCTGCAAGAGACTTCCATC and (antisense) 5'
536 GAAGTCCCTCTGCAAGAGACTTCCATC. Primer sequences for other transcripts
537 are available upon request and have been previously published (44-46). Primer
538 efficiency was calculated during qRT-PCR optimisation and an efficiency between 90–
539 110% was obtained for all primer pairs (data not shown). During data analysis,

540 amplification of each gene was normalised to GAPDH amplification. Fold change of
541 each gene was calculated relative to the empty vector transfected, poly(I:C) stimulated
542 control.

543

544 **EMCV reverse genetics**

545

546 The parental (WT) EMCV sequence has been previously described (3) and is based on
547 the EMCV subtype mengovirus cDNA, pMC0, developed by Ann Palmenberg
548 (University of Wisconsin-Madison) (47). It resembles GenBank accession DQ294633.1,
549 although the poly(C) tract is absent and there are 13 single-nucleotide differences
550 (A2669C, G3044C, C3371T, A4910C, G4991A, C5156T, G5289A, G5314C, G5315A,
551 A5844C, G6266A, G6990A, A6992G; DQ294633.1 coordinates). The 2B*KO mutation
552 in a subclone has been previously described (11). Regions encompassing the mutations
553 of interest were digested using *Bg*II and *Pacl* and ligated into the WT EMCV molecular
554 clone.

555

556 The GFP-Lzn EMCV clone was a kind gift from Prof. Frank van Kuppeveld and was
557 derived from the clone pRLuc-QG-M16.1 (13, 48). The Lzn mutation was mutated to WT
558 and the 2B*KO and GNN mutations were subsequently introduced (primer sequences
559 available upon request). All GFP viral clones contain the EMCV IRES followed by the
560 first 6 codons of the viral protein L, followed by sequence encoding GFP inserted into
561 restriction enzyme cloning sites. The viral 3C protease cleavage site Gln-Gly
562 immediately precedes the full-length viral polyprotein coding sequence, including L but

563 without the initiation methionine, allowing the GFP to be separated from L. Sanger
564 sequencing was used to sequence the full length of all mutant and WT viral clones
565 (Biochemistry Sequencing Facility, University of Cambridge).

566

567 EMCV molecular clones were linearised with *BamH*I and genomic RNA was *in vitro*
568 transcribed using the T7 RiboMax kit (Promega). Transcripts were purified (RNeasy kit,
569 Qiagen) before being transfected into BHK-21 cells to generate virus stocks.

570

571 Preparation of virus stocks

572

573 BHK-21 cells were grown to 60–70% confluence in 10 cm dishes. All Opti-MEM (Gibco)
574 was supplemented with 1:1000 RNaseOUT (Invitrogen). 90 µL lipofectamine 2000
575 (Invitrogen) was added to 1.8 mL Opti-MEM and 14 µg RNA was added to another 1.8
576 mL Opti-MEM. These solutions were mixed together and incubated for 20 min while
577 cells were washed with PBS. Following addition of transfection mixture, cells were
578 incubated for 3.5 h at room temperature with gentle agitation. Transfection medium was
579 removed prior to the addition of 8 mL of 2% FCS DMEM and incubation for 24 h or until
580 full CPE was visible. The plates were then scraped and samples freeze/thawed thrice,
581 prior to the dead cells and debris being removed by light clarification and the
582 supernatant frozen at –70°C in aliquots. Virus concentration was estimated by plaque
583 assay.

584

585 Plaque assays

586

587 BSR cells were seeded at 35% confluence in 6 well plates 24 h prior to infection.
588 The media was removed and the cells were washed once with PBS before the addition
589 of 1 mL sera-free DMEM containing the specified dilution of virus. The infection was
590 incubated at room temperature with continuous rocking for 1 h before the inocula was
591 removed, the cells were washed once with PBS and 3 mL of DMEM (2% FCS)
592 containing 1% low melting point agarose (ThermoFisher Scientific) was added to each
593 well. Cells were incubated for 48 h before being fixed with 4% formaldehyde and
594 stained with toluidine blue. Plaques were counted manually and their sizes quantified
595 using ImageJ (49, 50).

596

597 Immunoblots

598

599 During validation of 2B*KO EMCV, all samples to be analysed by immunoblot were
600 frozen in RIPA buffer (ThermoFisher Scientific) containing 1:10,000 Benzonase
601 nuclease (Sigma) and protease and phosphatase inhibitors (Halt, ThermoFisher
602 Scientific) (“complete RIPA”). All samples were boiled in SDS-based protein loading dye
603 (Laemmli buffer) containing 10 mM DTT for 7 min prior to electrophoresis. Following
604 resolution, proteins were transferred to 0.2 µm nitrocellulose membranes by semi-dry
605 electrotransfer in a Transblot turbo transfer system using recommended standard
606 settings (Bio-Rad). Membranes were blocked with 5% w/v non-fat milk powder in PBS
607 for a minimum of 3 h with continuous rocking. Primary antibodies were diluted in
608 blocking buffer prior to incubation with the membrane for at least 2 h. Membranes were

609 washed 3 times with TBS-Tween20 (0.1%) before being incubated with the relevant
610 secondary antibody for 1 h with continuous rocking. Membranes were again washed 3
611 times with TBS-Tween20 (0.1%) before being imaged with the Odyssey CLx imaging
612 system (LI-COR).

613

614 Quantitative proteomics and TMT labelling of co-immunoprecipitation samples from
615 infected BHK-21 cells

616

617 BHK-21 cells were mock infected or infected with HA tagged WT and HA tagged 2B*KO
618 EMCV at an MOI 5.0 for 10 hpi in five, 10cm dishes per sample, each in triplicate. Due
619 to the number of dishes, samples were separated into two groups and infected one hour
620 apart to ensure the number of IP samples would be manageable. The HA tagged 2B*
621 was then purified using the Pierce Magnetic HA-Tag IP/Co-IP Kit with wash buffer
622 supplemented with Halt protease and phosphatase inhibitors (ThermoFisher Scientific).
623 During the final wash, 12.5% of each sample was retained in separate tubes for western
624 blot analysis. Following the removal of the buffer for the third and final wash from the
625 rest of the sample, the beads were snap frozen. Samples were eluted from the beads
626 by boiling in 2x SDS Loading buffer and prepared for downstream proteomic analysis by
627 SP3 sample preparation (51). In brief, samples were reduced and alkylated, followed by
628 precipitation onto magnetic beads by the addition of ethanol to 80% (v/v) final
629 concentration. Samples were then washed three times in 90% (v/v) ethanol, and then
630 resuspended in 100mM TEAB containing 20ng/uL Trypsin Gold and digested overnight.
631 Following digestion, samples were removed from the beads and labelled with Tandem

632 Mass Tag reagents (ThermoFisher Scientific), before quenching with the addition of
633 hydroxylamine. Samples were desalted by stage-tipping before analysis by LC-MS/MS
634 on a Dionex 3000 coupled in line to a Q-Exactive-HF mass spectrometer using data-
635 dependent acquisition. Analysis was performed using MaxQuant (52) using a fasta file
636 containing Syrian Golden Hamster and EMCV protein sequences. Raw data and the
637 .fasta files used have been uploaded to the PRIDE repository [accession number
638 pending] (53).

639

640 Downstream data analysis of the MaxQuant proteinGroups output file was conducted
641 using Perseus 2.0.11 (54). Reverse database hits, common contaminants (MaxQuant
642 contaminant list) and proteins only identified by site were removed. Data were
643 normalised for equal protein loading based on the median total reporter intensity and
644 then subjected to a $\log_2(x)$ transformation. Replicate samples were grouped and rows
645 with < 3 valid values in at least one group were removed. Missing data were imputed
646 from the normal distribution before Student's *t*-tests. Putative interaction partners were
647 defined as having both $-\log_{10}(p\text{-value})$ greater than 1.3 (*p*-value >0.05) and fold change
648 of greater than 2 ($\log_2(\text{Fold change}) > 1$) in both the comparison of HA2B* EMCV vs
649 mock and HA2B* EMCV vs HA2B*KO EMCV.

650

651 Anti-FLAG immunoprecipitation

652

653 BHK-21 cells were co-transfected with both pCAGG-HA2B* and a cloned FLAG-tagged
654 putative interaction partner (pCAGG-X) in 10 cm dishes. 24 h after transfection, the cells

655 were washed in ice cold PBS before being scraped and lysed in 750 μ L of lysis buffer
656 (25 mM Tris HCl [pH 7.4], 150 mM NaCl, 1 mM EDTA, 1% NP40, 5% glycerol, pH 7.4)
657 for 10 min at 4°C. The lysates were clarified and 50 μ L was retained (input). The FLAG-
658 tagged bait protein and any interacting proteins were purified using anti-FLAG resin
659 (Sigma). Briefly, lysates were incubated with the resin with continuous rotation for a
660 minimum of 2 h at 4°C, then washed thrice in fresh lysis buffer. Following the removal of
661 the final wash, the resin was boiled for 5 min in 60 μ L 2x protein loading dye (Laemmli
662 buffer) in the absence of DTT. The undissolved resin was removed by centrifugation
663 and DTT was added (final concentration 5 mM) prior to reheating the sample for a
664 further 3 min. Proteins were resolved by polyacrylamide gel electrophoresis and imaged
665 by immunoblot against the epitope tags.

666

667 Confocal microscopy

668

669 BSR cells were seeded at 20% confluence on to glass coverslips in 24 well plates, 24 h
670 prior to transfection (see above). 24 h after transfection, cells were washed in PBS and
671 fixed with 4% paraformaldehyde for 20 min at room temperature. Cells were washed
672 thrice both prior to and immediately following permeabilisation with 0.5% Triton X-100
673 for 10 min. To reduce nonspecific binding, cells were blocked with 10% BSA for a
674 minimum of 2 h at room temperature with gentle agitation before addition of the relevant
675 primary antibodies. Antibodies against the HA epitope (C29F4, Cell Signaling
676 Technologies) and the FLAG epitope (F1804, Sigma) were each diluted 1:1000 and the
677 coverslips were incubated at 4°C overnight with continuous gentle rocking. Samples

678 were thrice washed in PBS before the addition of fluorophore-labelled secondary
679 antibodies diluted in 10% BSA (anti-rabbit Alexa-fluor 488 (Invitrogen); anti-rat Alexa-
680 fluor 594 (abcam)). Samples were again incubated with continuous rocking at room
681 temperature for 1 h. Finally, samples were thrice washed and the coverslips were
682 mounted upon glass slides. DAPI was included in the mounting media (Prolong gold
683 antifade with DAPI, ThermoFisher Scientific). Samples were imaged at 63 x on a LSM
684 700 laser scanning confocal microscope.

685

686 Live cell imaging

687

688 BHK-21 cells infected with GFP-tagged viruses were imaged at regular intervals using
689 the Incucyte live cell analysis system and the Incucyte 2022B Rev2 GUI software
690 (Sartorius). Three regions were imaged per well using a 10x objective (96 well plate,
691 each sample in technical triplicate). The background threshold for each plate was
692 independently set using manually selected images, with high and low fluorescence
693 levels. Cell confluence was measured by phase microscopy. GCU at each time point
694 was normalised to the respective GCU in that well at 5.5 h post infection.

695

696 In silico protein modelling

697

698 Alphafold (55), I-TASSER (56) and NetSurfp 3.0 (57) were used to predict the
699 secondary structure of 2B*, using the amino acid sequence from GenBank accession
700 DQ294633.1.

701

702 **ACKNOWLEDGEMENTS**

703 The authors would like to thank Prof. Frank J.M. van Kuppeveld (Utrecht University) for
704 kindly providing a molecular clone of GFP-tagged EMCV. The authors would like to
705 thank Prof. Ian Brierley, Prof. Colin Crump and Prof. Stephen Graham (University of
706 Cambridge) for useful discussions, as well as Prof. Ann Palmenberg (University of
707 Wisconsin-Madison) for providing additional supporting reagents. A.E.F. and H.S. were
708 supported by Wellcome Trust Senior Research Fellowships (106207/Z/14/Z,
709 220814/Z/20/Z) and a European Research Council grant (646891). J.R.E. was
710 supported by a Sir Henry Dale Fellowship jointly funded by the Wellcome Trust and the
711 Royal Society (216370/Z/19/Z). EE and SH are supported by funding from the Academy
712 of Medical Sciences (SBF006\1008), the Medical Research Council (MR/X000885/1),
713 and a Wellcome Trust Career Development Award (227831/Z/23/Z) awarded to EE.
714 S.K.N. was supported by a Department of Pathology, University of Cambridge PhD
715 studentship that was funded by the Waldmann Fund. The funders had no role in study
716 design or data interpretation, or the decision to submit the work for publication. For the
717 purposes of open access, the authors have applied a CC BY public copyright licence to
718 any Author Accepted article version arising from this submission. Figure 6 was created
719 with BioRender.com and is published under Agreement Number ZR26VGQ7I.

720 Author Contributions: S.K.N., H.S. and A.E.F. designed the study and experiments.
721 S.K.N., E.E., N.L., L.G.C. and S.H. performed experiments. H.S., J.R.E., H.B., I.G.,
722 A.S.J., E.E. and A.E.F. provided expertise on data analysis, interpretation and

723 methodology. S.K.N. and H.S. wrote the article. All authors edited and discussed the
724 article. A.E.F., J.R.E. and E.E. secured funding.

725

726 **REFERENCES**

727

728 1. Loughran G, Libbey JE, Uddowla S, Scallan MF, Ryan MD, Fujinami RS, Rieder
729 E, Atkins JF. 2013. Theiler's murine encephalomyelitis virus contrasts with
730 encephalomyocarditis and foot-and-mouth disease viruses in its functional utilization of
731 the StopGo non-standard translation mechanism. *J Gen Virol* 94:348-353.

732 2. Loughran G, Firth AE, Atkins JF. 2011. Ribosomal frameshifting into an
733 overlapping gene in the 2B-encoding region of the cardiovirus genome. *Proc Natl Acad
734 Sci U S A* 108:E1111-9.

735 3. Napthine S, Ling R, Finch LK, Jones JD, Bell S, Brierley I, Firth AE. 2017.
736 Protein-directed ribosomal frameshifting temporally regulates gene expression. *Nat
737 Commun* 8:15582.

738 4. Hill CH, Pekarek L, Napthine S, Kibe A, Firth AE, Graham SC, Caliskan N,
739 Brierley I. 2021. Structural and molecular basis for Cardiovirus 2A protein as a viral
740 gene expression switch. *Nat Commun* 12:7166.

741 5. Finch LK, Ling R, Napthine S, Olspert A, Michiels T, Lardinois C, Bell S,
742 Loughran G, Brierley I, Firth AE. 2015. Characterization of Ribosomal Frameshifting in
743 Theiler's Murine Encephalomyelitis Virus. *J Virol* 89:8580-9.

744 6. Hill CH, Cook GM, Napthine S, Kibe A, Brown K, Caliskan N, Firth AE, Graham
745 SC, Brierley I. 2021. Investigating molecular mechanisms of 2A-stimulated ribosomal
746 pausing and frameshifting in Theilovirus. Nucleic Acids Res 49:11938-11958.

747 7. Tam EH, Liu YC, Woung CH, Liu HM, Wu GH, Wu CC, Kuo RL. 2021. Role of
748 the Chaperone Protein 14-3-3epsilon in the Regulation of Influenza A Virus-Activated
749 Beta Interferon. J Virol 95:e0023121.

750 8. Riedl W, Acharya D, Lee JH, Liu G, Serman T, Chiang C, Chan YK, Diamond
751 MS, Gack MU. 2019. Zika Virus NS3 Mimics a Cellular 14-3-3-Binding Motif to
752 Antagonize RIG-I- and MDA5-Mediated Innate Immunity. Cell Host Microbe 26:493-503
753 e6.

754 9. Gupta S, Yla-Anttila P, Sandalova T, Sun R, Achour A, Masucci MG. 2019. 14-3-
755 3 scaffold proteins mediate the inactivation of trim25 and inhibition of the type I
756 interferon response by herpesvirus deconjugases. PLoS Pathog 15:e1008146.

757 10. Andrews DDT, Vlok M, Akbari Bani D, Hay BN, Mohamud Y, Foster LJ, Luo H,
758 Overall CM, Jan E. 2023. Cleavage of 14-3-3epsilon by the enteroviral 3C protease
759 dampens RIG-I-mediated antiviral signaling. J Virol 97:e0060423.

760 11. Ling R, Firth AE. 2017. An analysis by metabolic labelling of the
761 encephalomyocarditis virus ribosomal frameshifting efficiency and stimulators. J Gen
762 Virol 98:2100-2105.

763 12. Loughran G, Howard MT, Firth AE, Atkins JF. 2017. Avoidance of reporter assay
764 distortions from fused dual reporters. RNA 23:1285-1289.

765 13. Dorobantu CM, Albulescu L, Harak C, Feng Q, van Kampen M, Strating JR,
766 Gorbatenya AE, Lohmann V, van der Schaar HM, van Kuppeveld FJ. 2015. Modulation

767 of the Host Lipid Landscape to Promote RNA Virus Replication: The Picornavirus
768 Encephalomyocarditis Virus Converges on the Pathway Used by Hepatitis C Virus.
769 PLoS Pathog 11:e1005185.

770 14. Pennington KL, Chan TY, Torres MP, Andersen JL. 2018. The dynamic and
771 stress-adaptive signaling hub of 14-3-3: emerging mechanisms of regulation and
772 context-dependent protein-protein interactions. Oncogene 37:5587-5604.

773 15. Liou JY, Ghelani D, Yeh S, Wu KK. 2007. Nonsteroidal anti-inflammatory drugs
774 induce colorectal cancer cell apoptosis by suppressing 14-3-3epsilon. Cancer Res
775 67:3185-91.

776 16. Hermeking H, Benzinger A. 2006. 14-3-3 proteins in cell cycle regulation. Semin
777 Cancer Biol 16:183-92.

778 17. Zhao S, Li B, Li C, Gao H, Miao Y, He Y, Wang H, Gong L, Li D, Zhang Y, Feng
779 J. 2019. The Apoptosis Regulator 14-3-3eta and Its Potential as a Therapeutic Target in
780 Pituitary Oncocytoma. Front Endocrinol (Lausanne) 10:797.

781 18. Eckardt NA. 2001. Transcription factors dial 14-3-3 for nuclear shuttle. Plant Cell
782 13:2385-9.

783 19. Lin JP, Fan YK, Liu HM. 2019. The 14-3-3eta chaperone protein promotes
784 antiviral innate immunity via facilitating MDA5 oligomerization and intracellular
785 redistribution. PLoS Pathog 15:e1007582.

786 20. Liu HM, Loo YM, Horner SM, Zornetzer GA, Katze MG, Gale M, Jr. 2012. The
787 mitochondrial targeting chaperone 14-3-3epsilon regulates a RIG-I translocon that
788 mediates membrane association and innate antiviral immunity. Cell Host Microbe
789 11:528-37.

790 21. Jia H, Liang Z, Zhang X, Wang J, Xu W, Qian H. 2017. 14-3-3 proteins: an
791 important regulator of autophagy in diseases. *Am J Transl Res* 9:4738-4746.

792 22. Gu Y, Xu K, Torre C, Samur M, Barwick BG, Rupji M, Arora J, Neri P, Kaufman
793 J, Nooka A, Bernal-Mizrachi L, Vertino P, Sun SY, Chen J, Munshi N, Fu H, Kowalski J,
794 Boise LH, Lonial S. 2018. 14-3-3zeta binds the proteasome, limits proteolytic function
795 and enhances sensitivity to proteasome inhibitors. *Leukemia* 32:744-751.

796 23. Kumar M, Michael S, Alvarado-Valverde J, Meszaros B, Samano-Sanchez H,
797 Zeke A, Dobson L, Lazar T, Ord M, Nagpal A, Farahi N, Kaser M, Kraleti R, Davey NE,
798 Pancsa R, Chemes LB, Gibson TJ. 2022. The Eukaryotic Linear Motif resource: 2022
799 release. *Nucleic Acids Res* 50:D497-D508.

800 24. Coblitz B, Wu M, Shikano S, Li M. 2006. C-terminal binding: an expanded
801 repertoire and function of 14-3-3 proteins. *FEBS Lett* 580:1531-5.

802 25. Muslin AJ, Tanner JW, Allen PM, Shaw AS. 1996. Interaction of 14-3-3 with
803 signaling proteins is mediated by the recognition of phosphoserine. *Cell* 84:889-97.

804 26. Gack MU, Shin YC, Joo CH, Urano T, Liang C, Sun L, Takeuchi O, Akira S,
805 Chen Z, Inoue S, Jung JU. 2007. TRIM25 RING-finger E3 ubiquitin ligase is essential
806 for RIG-I-mediated antiviral activity. *Nature* 446:916-920.

807 27. Reikine S, Nguyen JB, Modis Y. 2014. Pattern Recognition and Signaling
808 Mechanisms of RIG-I and MDA5. *Front Immunol* 5:342.

809 28. Seth RB, Sun L, Ea CK, Chen ZJ. 2005. Identification and characterization of
810 MAVS, a mitochondrial antiviral signaling protein that activates NF-kappaB and IRF 3.
811 *Cell* 122:669-82.

812 29. Li L, Fan H, Song Z, Liu X, Bai J, Jiang P. 2019. Encephalomyocarditis virus 2C
813 protein antagonizes interferon-beta signaling pathway through interaction with MDA5.
814 Antiviral Res 161:70-84.

815 30. Hato SV, Ricour C, Schulte BM, Lanke KH, de Bruijini M, Zoll J, Melchers WJ,
816 Michiels T, van Kuppeveld FJ. 2007. The mengovirus leader protein blocks interferon-
817 alpha/beta gene transcription and inhibits activation of interferon regulatory factor 3. Cell
818 Microbiol 9:2921-30.

819 31. Stavrou S, Feng Z, Lemon SM, Roos RP. 2010. Different strains of Theiler's
820 murine encephalomyelitis virus antagonize different sites in the type I interferon
821 pathway. J Virol 84:9181-9.

822 32. Manivannan P, Siddiqui MA, Malathi K. 2020. RNase L Amplifies Interferon
823 Signaling by Inducing Protein Kinase R-Mediated Antiviral Stress Granules. J Virol 94.

824 33. Drappier M, Jha BK, Stone S, Elliott R, Zhang R, Vertommen D, Weiss SR,
825 Silverman RH, Michiels T. 2018. A novel mechanism of RNase L inhibition: Theiler's
826 virus L* protein prevents 2-5A from binding to RNase L. PLoS Pathog 14:e1006989.

827 34. Brunet A, Kanai F, Stehn J, Xu J, Sarbassova D, Frangioni JV, Dalal SN,
828 DeCaprio JA, Greenberg ME, Yaffe MB. 2002. 14-3-3 transits to the nucleus and
829 participates in dynamic nucleocytoplasmic transport. J Cell Biol 156:817-28.

830 35. Jen G, Thach RE. 1982. Inhibition of host translation in encephalomyocarditis
831 virus-infected L cells: a novel mechanism. J Virol 43:250-61.

832 36. Bustos DM. 2012. The role of protein disorder in the 14-3-3 interaction network.
833 Mol Biosyst 8:178-84.

834 37. Rogers KJ, Jones-Burrage S, Maury W, Mukhopadhyay S. 2020. TF protein of
835 Sindbis virus antagonizes host type I interferon responses in a palmitoylation-dependent
836 manner. *Virology* 542:63-70.

837 38. Khalil AM, Nogales A, Martinez-Sobrido L, Mostafa A. 2024. Antiviral responses
838 versus virus-induced cellular shutoff: a game of thrones between influenza A virus NS1
839 and SARS-CoV-2 Nsp1. *Front Cell Infect Microbiol* 14:1357866.

840 39. Zhang B, Liu M, Huang J, Zeng Q, Zhu Q, Xu S, Chen H. 2022. H1N1 Influenza
841 A Virus Protein NS2 Inhibits Innate Immune Response by Targeting IRF7. *Viruses* 14.

842 40. da Costa LS, Outlioua A, Anginot A, Akarid K, Arnoult D. 2019. RNA viruses
843 promote activation of the NLRP3 inflammasome through cytopathogenic effect-induced
844 potassium efflux. *Cell Death Dis* 10:346.

845 41. Schwarz EM, Badorff C, Hiura TS, Wessely R, Badorff A, Verma IM, Knowlton
846 KU. 1998. NF-kappaB-mediated inhibition of apoptosis is required for
847 encephalomyocarditis virus virulence: a mechanism of resistance in p50 knockout mice.
848 *J Virol* 72:5654-60.

849 42. Li Y, Shang P, Shyu D, Carrillo C, Naraghi-Arani P, Jaing CJ, Renukaradhya GJ,
850 Firth AE, Snijder EJ, Fang Y. 2018. Nonstructural proteins nsp2TF and nsp2N of
851 porcine reproductive and respiratory syndrome virus (PRRSV) play important roles in
852 suppressing host innate immune responses. *Virology* 517:164-176.

853 43. Pavesi A. 2021. Origin, Evolution and Stability of Overlapping Genes in Viruses:
854 A Systematic Review. *Genes (Basel)* 12.

855 44. Jahun AS, Sorgeloos F, Chaudhry Y, Arthur SE, Hosmillo M, Georgana I,
856 Izuagbe R, Goodfellow IG. 2023. Leaked genomic and mitochondrial DNA contribute to
857 the host response to noroviruses in a STING-dependent manner. *Cell Rep* 42:112179.

858 45. Petro TM. 2005. ERK-MAP-kinases differentially regulate expression of IL-23 p19
859 compared with p40 and IFN-beta in Theiler's virus-infected RAW264.7 cells. *Immunol
860 Lett* 97:47-53.

861 46. Wu Y, Li YY, Matsushima K, Baba T, Mukaida N. 2008. CCL3-CCR5 axis
862 regulates intratumoral accumulation of leukocytes and fibroblasts and promotes
863 angiogenesis in murine lung metastasis process. *J Immunol* 181:6384-93.

864 47. Duke GM, Osorio JE, Palmenberg AC. 1990. Attenuation of Mengo virus through
865 genetic engineering of the 5' noncoding poly(C) tract. *Nature* 343:474-6.

866 48. Albulescu L, Wubbolts R, van Kuppeveld FJ, Strating JR. 2015. Cholesterol
867 shuttling is important for RNA replication of coxsackievirus B3 and
868 encephalomyocarditis virus. *Cell Microbiol* 17:1144-56.

869 49. Schindelin J, Arganda-Carreras I, Frise E, Kaynig V, Longair M, Pietzsch T,
870 Preibisch S, Rueden C, Saalfeld S, Schmid B, Tinevez JY, White DJ, Hartenstein V,
871 Eliceiri K, Tomancak P, Cardona A. 2012. Fiji: an open-source platform for biological-
872 image analysis. *Nat Methods* 9:676-82.

873 50. Rueden CT, Schindelin J, Hiner MC, DeZonia BE, Walter AE, Arena ET, Eliceiri
874 KW. 2017. ImageJ2: ImageJ for the next generation of scientific image data. *BMC
875 Bioinformatics* 18:529.

876 51. Hughes CS, Mogridge S, Muller T, Sorensen PH, Morin GB, Krijgsveld J. 2019.
877 Single-pot, solid-phase-enhanced sample preparation for proteomics experiments. *Nat*
878 *Protoc* 14:68-85.

879 52. Tyanova S, Temu T, Cox J. 2016. The MaxQuant computational platform for
880 mass spectrometry-based shotgun proteomics. *Nat Protoc* 11:2301-2319.

881 53. Perez-Riverol Y, Bai J, Bandla C, Garcia-Seisdedos D, Hewapathirana S,
882 Kamatchinathan S, Kundu DJ, Prakash A, Frericks-Zipper A, Eisenacher M, Walzer M,
883 Wang S, Brazma A, Vizcaino JA. 2022. The PRIDE database resources in 2022: a hub
884 for mass spectrometry-based proteomics evidences. *Nucleic Acids Res* 50:D543-D552.

885 54. Tyanova S, Temu T, Sinitcyn P, Carlson A, Hein MY, Geiger T, Mann M, Cox J.
886 2016. The Perseus computational platform for comprehensive analysis of (prote)omics
887 data. *Nat Methods* 13:731-40.

888 55. Jumper J, Evans R, Pritzel A, Green T, Figurnov M, Ronneberger O,
889 Tunyasuvunakool K, Bates R, Zidek A, Potapenko A, Bridgland A, Meyer C, Kohl SAA,
890 Ballard AJ, Cowie A, Romera-Paredes B, Nikolov S, Jain R, Adler J, Back T, Petersen
891 S, Reiman D, Clancy E, Zielinski M, Steinegger M, Pacholska M, Berghammer T,
892 Bodenstein S, Silver D, Vinyals O, Senior AW, Kavukcuoglu K, Kohli P, Hassabis D.
893 2021. Highly accurate protein structure prediction with AlphaFold. *Nature* 596:583-589.

894 56. Yang J, Yan R, Roy A, Xu D, Poisson J, Zhang Y. 2015. The I-TASSER Suite:
895 protein structure and function prediction. *Nat Methods* 12:7-8.

896 57. Hoie MH, Kiehl EN, Petersen B, Nielsen M, Winther O, Nielsen H, Hallgren J,
897 Marcatili P. 2022. NetSurfP-3.0: accurate and fast prediction of protein structural

898 features by protein language models and deep learning. Nucleic Acids Res 50:W510-
899 W515.

900

901 **FIGURE TITLES AND LEGENDS**

902

903 **Figure 1: 2B*KO EMCV mutations do not impact viral frameshifting or replication.**

904 **(A)** Schematic representation of the dual luciferase constructs. Renilla luciferase is
905 produced by every translating ribosome. However, in the WT sequence, firefly luciferase
906 is only produced when frameshifting does not occur. This enables quantitative
907 measurement of the percentage of ribosomes in each reading frame for each mutant
908 construct. **(B)** BHK-21 cells were transiently co-transfected with a WT EMCV 2A
909 expression construct (pCAGG-2A) along with a dual luciferase plasmid containing 105
910 nt of the EMCV genome (WT pSGDLuc) or mutants thereof (2B*KO pSGDLuc, SS-SL
911 pSGDLuc or -1 SS-SL pSGDLuc) at various ratios. At 24 h post-transfection, cells were
912 frozen in 1x PLB and both renilla and firefly luciferase activities were measured.
913 Samples were normalised to the luciferase values for the same pSGDLuc construct co-
914 transfected with pCAGG-2A^{mut}. The percentages of ribosomes in the 0 or -1 reading
915 frames for each ratio of pCAGG-2A:pSGDLuc were calculated. Data shown are the
916 mean +/- SD of three biological repeats, each using triplicate wells. Statistical analysis
917 (Student's *t*-test): ns = not significant, * *p* ≤ 0.05, ** *p* ≤ 0.01. **(C)** A confluent monolayer
918 of BHK-21 cells was infected with GFP WT EMCV or the indicated mutants at MOI 0.01.
919 GCU was analysed using the Incuyte live-cell imaging suite (Sartorius) and normalised
920 to respective GCU at 5.5 h p.i. Data shown are the mean +/- SD of three biological

921 repeats, each using triplicate wells. Statistical analysis (Student's t-test of the indicated
922 virus compared to GFP WT EMCV): ns = not significant, * $p \leq 0.05$.

923

924 **Figure 2: Characterisation of HA2B* EMCV. (A)** Schematic representation of the
925 EMCV viral genome with sequence encoding the HA tag inserted to tag 2B*. **(B)** BHK-
926 21 cells were infected with WT EMCV, 2B*KO EMCV, HA2B* EMCV or HA2B*KO
927 EMCV at MOI 5.0. Cells were harvested at the indicated time points, and frozen in
928 complete RIPA buffer. Lysates were subjected to SDS-PAGE and immunoblotting. The
929 membrane was cut at the 25 kDa marker on the ladder to allow the same membrane to
930 be probed by all four antibodies. The molecular mass scale (kDa) is indicated at left and
931 antibodies used are labelled at right. **(C)** Images of plaques formed by the viruses
932 indicated, grown in BSR cells. Images are representative of three independent
933 biological repeats. **(D)** Size distribution of plaques formed by WT EMCV, HA2B* EMCV,
934 and their respective 2B*KO mutants. Distributions shown are based on area
935 measurements of 30 plaques, sampled from three biological repeats. Horizontal lines
936 represent the median (dashed) and upper and lower quartiles (dotted). Statistical
937 analysis (ratio-paired *t*-test): **** $p \leq 0.0001$.

938

939 **Figure 3: Putative interaction partners of 2B* include the entire family of 14-3-3**
940 **proteins. (A)** Schematic diagram of the TMT experiment. BHK-21 cells were infected
941 with either HA2B* EMCV or HA2B*KO EMCV, or mock infected. At 7 h p.i., HA2B*
942 along with any interaction partners were purified from the lysates by anti-HA co-
943 immunoprecipitation; 87.5% of each sample was then used for trypsin digestion, TMT

944 labelling and analysis by mass spectrometry. **(B)** The remaining 12.5% of each co-
945 immunoprecipitated sample was probed for HA-tagged proteins by western blot using
946 an anti-HA antibody. The molecular mass scale (kDa) is indicated at left and HA-tagged
947 proteins are labelled at right. **(C)** and **(D)** Two-sample *t*-tests were used to compare
948 protein enrichment in the HA2B* EMCV infected samples relative to HA2B*KO EMCV
949 infected samples (panel C) and mock infected samples (panel D). The $-\log_{10}(p\text{-value})$
950 greater than 1.3 (*p*-value >0.05) and fold change of greater than 2 ($\log_2(\text{Fold change}) >$
951 1) for each recognised protein are shown. Candidate interaction partners were defined
952 as those with both a Difference greater than 1 and a $-\log_2(p\text{-value})$ greater than 1.3.
953 Only proteins which were above these thresholds in the specified comparison are
954 labelled on the graph (red).

955

956 **Figure 4: 2B* binds to the entire family of 14-3-3 proteins via a C-terminal RRNSS**
957 **sequence. (A)** BHK-21 cells were co-transfected with equal amounts of pCAGG-HA2B*
958 and the specified N-terminally FLAG-tagged 14-3-3 encoding plasmid (pCAGG-FLAG
959 14-3-3x), 24 h prior to immunoprecipitation via the FLAG epitope. Samples were then
960 subjected to SDS-PAGE and immunoblotting using the indicated antibodies. Data
961 shown are representative of two independent biological repeats. **(B)** BHK-21 cells were
962 co-transfected with both a plasmid encoding either an N-terminally FLAG-tagged 14-3-3
963 protein or tubulin β chain and another encoding either HA Δ RRNSS2B* or HA2B*, as
964 indicated. Cell lysates were immunoprecipitated with anti-FLAG antibody and subjected
965 to SDS-PAGE and immunoblotting. Data shown are representative of two independent
966 biological repeats. **(C)** Confluent monolayers of BHK-21 cells were infected with WT

967 EMCV or Δ RRNSS 2B* EMCV at MOI 0.01. At 24 h p.i., RNA was extracted from each
968 sample and subjected to RT-PCR to amplify the region of interest. The cDNA was
969 sequenced (Sanger method) with both forward and reverse primers. Both
970 chromatograms have only one clear peak for each nucleotide, indicating each infected
971 sample contained only one EMCV sequence detectable by Sanger sequencing.
972 Chromatograms shown are representative of three independent biological repeats. (D)
973 BSR cells were infected with the indicated viruses 1 h prior to being overlaid with semi-
974 solid medium (1% LMA) for 48 h. Distributions shown are based on area measurements
975 of 60 randomly chosen plaques sampled over three biological repeats. Horizontal lines
976 represent the median (dashed) and upper and lower quartiles (dotted). Statistical
977 analysis (ratio-paired *t*-test): ** $p \leq 0.01$, **** $p \leq 0.0001$.

978

979 **Figure 5: Overexpressed 2B* interferes with innate immune signalling via its**
980 **interaction with 14-3-3 proteins. (A)** MEF cells were transiently transfected with
981 constructs encoding HA2B* or HA Δ RRNSS 2B*, or the empty vector, as indicated 24 h
982 prior to transfection with poly(I:C) (final concentration 10 ng/mL) for 6 h. The relative
983 expression level of each gene was determined by qRT-PCR. Expression levels were
984 normalised internally to GAPDH and to poly(I:C) stimulated samples transfected with
985 the empty vector (pCAGG). Data shown are the mean +/- SD of three biological
986 repeats. Statistical analysis (unpaired Welch *t*-test): ns = not significant, * $p \leq 0.05$, ** p
987 ≤ 0.01 .

988

989 **Figure 6:** Model of 2B* function. 2B* reduces NF κ B and IRF3 signalling likely by
990 inhibiting the translocation of innate immune signalling molecules MDA5, RIG-I and
991 TRIM25 by preventing their interactions with 14-3-3 proteins, thus reducing MAVS
992 activation.

993

994 **TABLE TITLES AND LEGENDS**

995 **Table 1:** Proteins which were statistically significantly enriched in HA2B* EMCV infected
996 samples relative to both HA2B*KO EMCV infected and mock infected samples.

997

998 **SUPPLEMENTAL MATERIAL**

999

1000 **Figure S1:** BSR cells were co-transfected with pCAGG-HA2B* and either the gene
1001 encoding 14-3-3 β or 14-3-3 γ , with an N-terminal FLAG tag, also in a pCAGG expression
1002 construct. Cells were fixed at 24 h and stained with both anti-HA and anti-FLAG
1003 antibodies. Nuclei were stained with DAPI during mounting. Images are representative
1004 of three independent biological repeats.

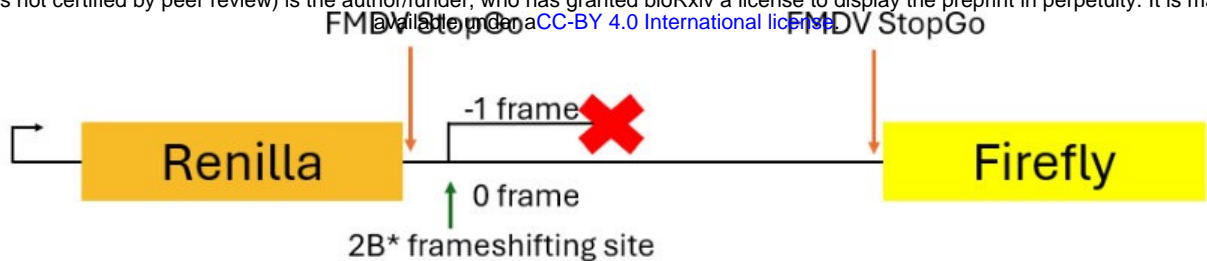
1005

1006 **Figure S2:** BSR cells were co-transfected with pCAGG-HA2B* and the gene encoding
1007 14-3-3 ϵ (isoform X1), 14-3-3 ζ or 14-3-3 η with an N-terminal FLAG tag, also in a pCAGG
1008 expression construct. Cells were fixed at 24 h and stained with both anti-HA and anti-
1009 FLAG antibodies. Nuclei were stained with DAPI during mounting. Images are
1010 representative of three independent biological repeats.

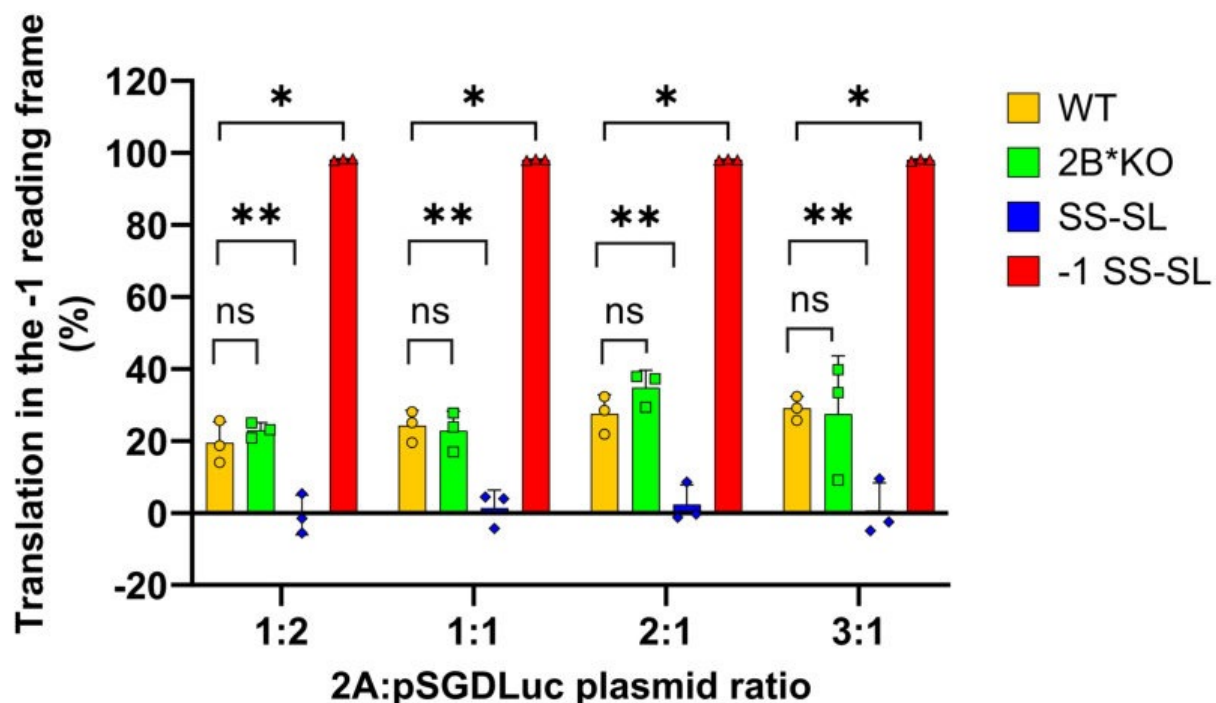
1011

1012 **Figure S3:** BSR cells were co-transfected with pCAGG-HA2B* and the gene encoding
1013 14-3-3 η , 14-3-3 θ or 14-3-3 σ , with an N-terminal FLAG tag, also in a pCAGG expression
1014 construct. Cells were fixed at 24 h and stained with both anti-HA and anti-FLAG
1015 antibodies. Nuclei were stained with DAPI during mounting. Images are representative
1016 of three independent biological repeats.
1017

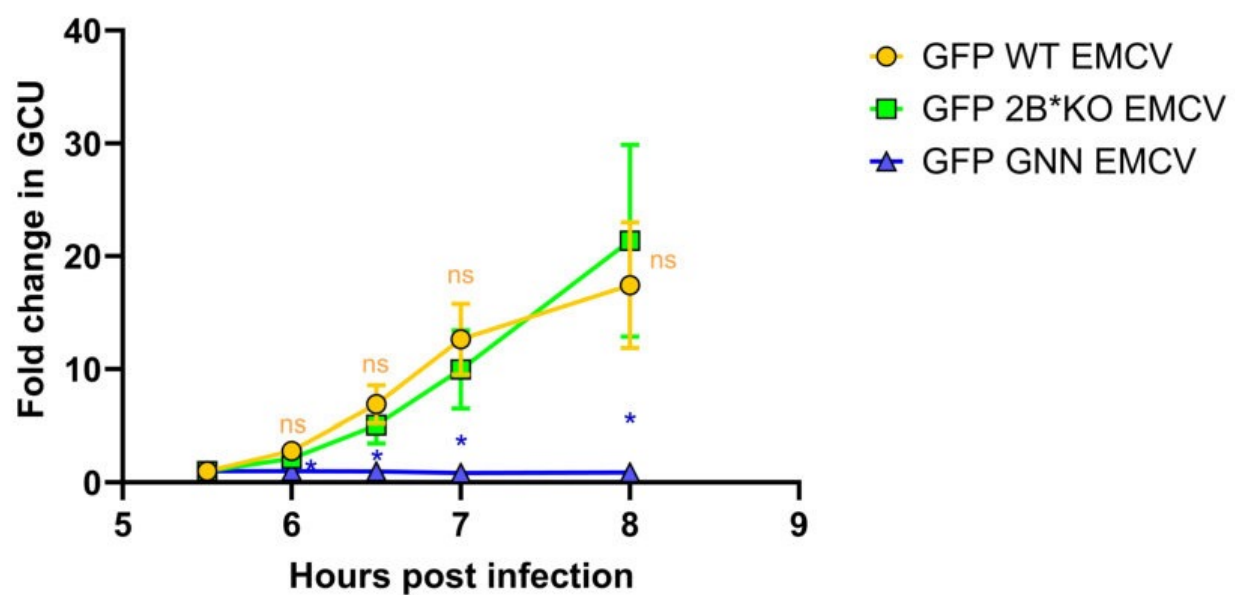
A

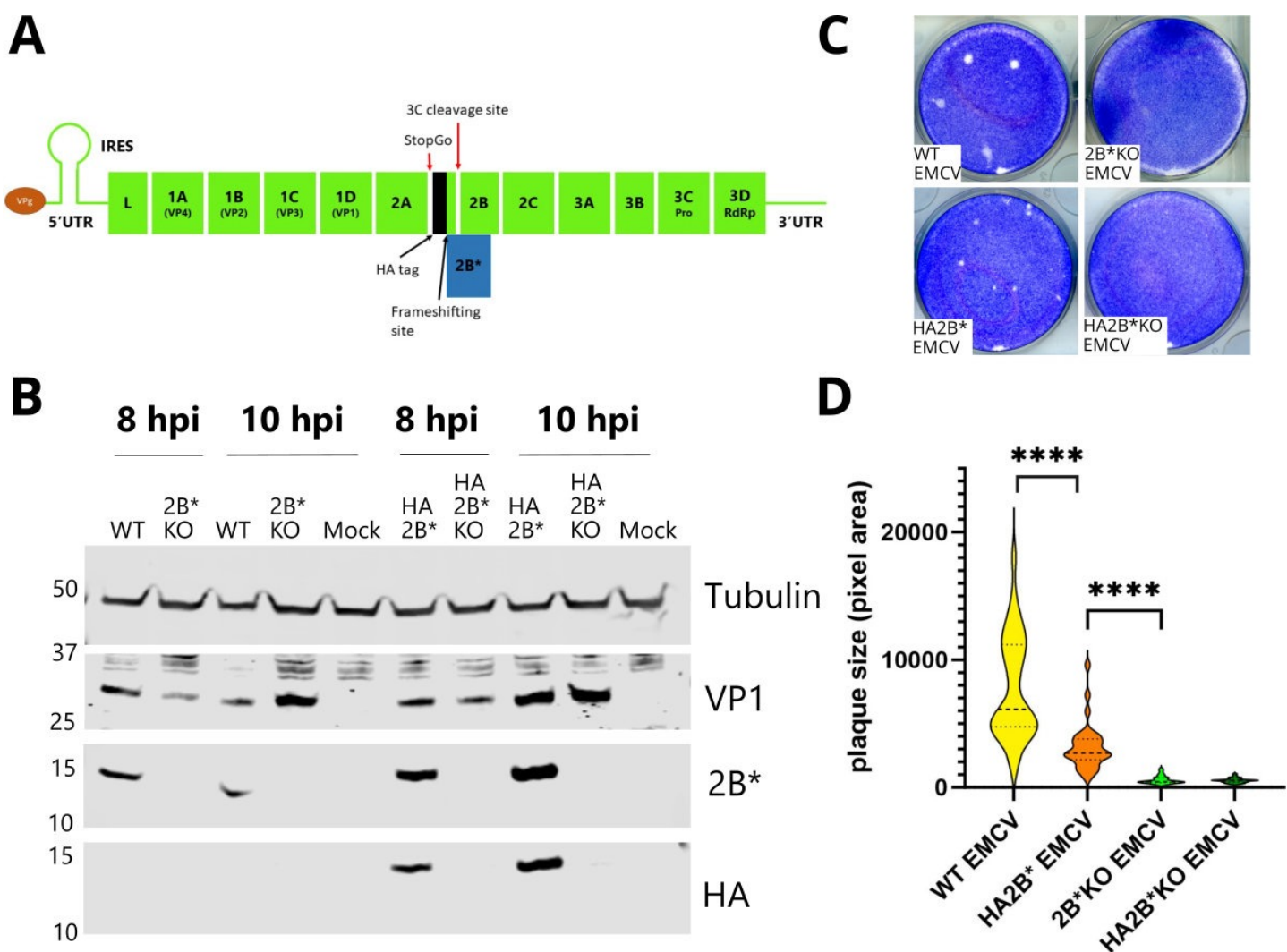


B

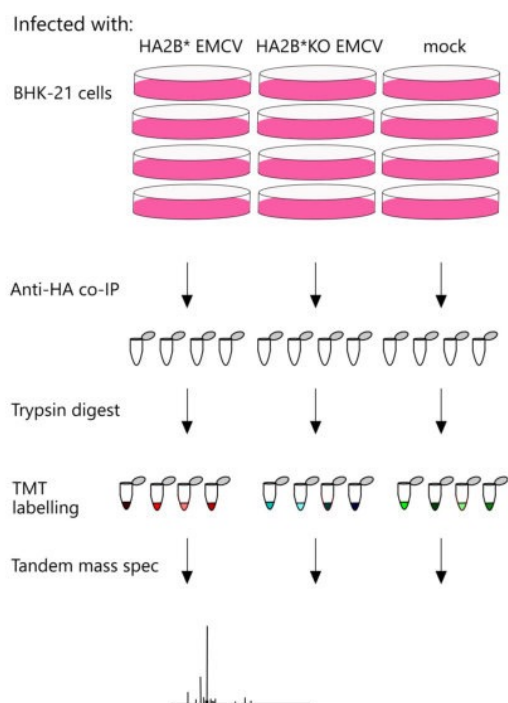


C

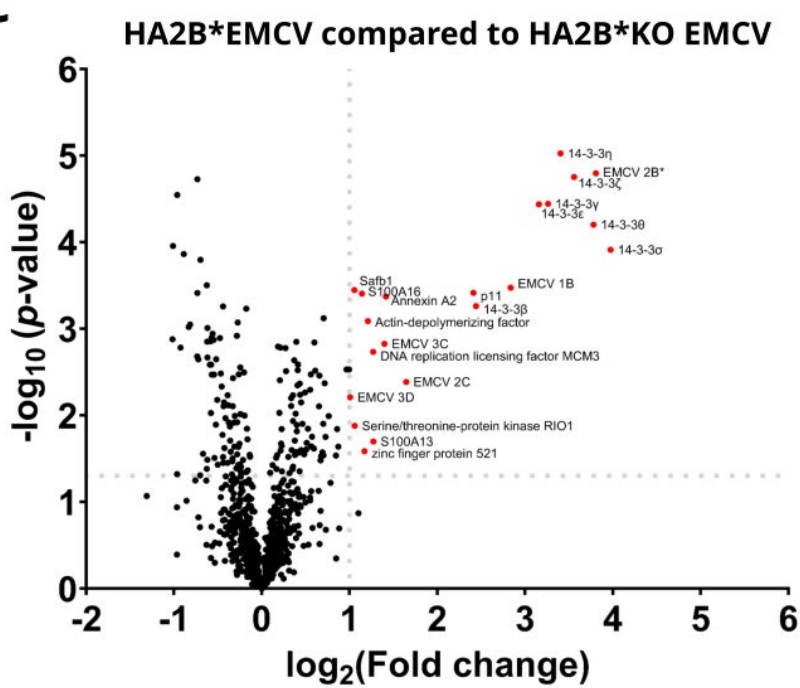




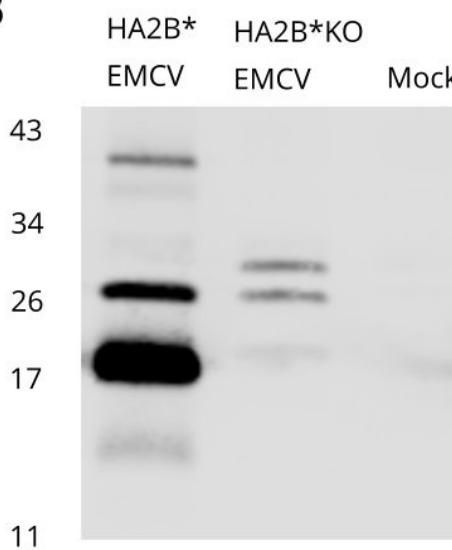
A



C



B



D

